Analytic signal phase-based myocardial motion estimation intagged MRI sequences by a bilinear model and motion compensation

Liang Wang, Adrian Basarab, Pascal Girard, P. Croisille, P. Clarysse, Philippe Delachartre

Analytic signal phase-based myocardial motion estimation in tagged MRI sequences by a bilinear model and motion compensation

Liang Wang[a], Adrian Basarab[b], Patrick R. Girard[a], Pierre Croisille[a], Patrick Clarysse[a], Philippe Delachartre[a]

[a] *Université de Lyon, CREATIS; CNRS UMR 5220; Inserm U1044; INSA-Lyon; Université Lyon 1. Bât. Blaise Pascal, 7 avenue Jean Capelle, F-69621 Villeurbanne, France*

[b] *Université de Toulouse; IRIT; CNRS UMR 5505; 118 Route de Narbonne, F-31062 Toulouse cedex 9, France*

Abstract

Different mathematical tools, such as multidimensional analytic signals, allow for the calculation of 2D spatial phases of real-value images. The motion estimation method proposed in this paper is based on two spatial phases of the 2D analytic signal applied to cardiac sequences. By combining the information of these phases issued from analytic signals of two successive frames, we propose an analytical estimator for 2D local displacements. To improve the accuracy of the motion estimation, a local bilinear deformation model is used within an iterative estimation scheme. The main advantages of our method are: (1) The phase-based method allows the displacement to be estimated with subpixel accuracy and is robust to image intensity variation in time; (2) Preliminary filtering is not required due to the bilinear model. Results from seven realistic simulated tagged magnetic resonance imaging (MRI) sequences show that our method is more accurate compared with state-of-the-art method for cardiac motion analysis and with another differential approach from the literature. The motion estimation errors (end point error) of the proposed method are reduced by about 33% compared with that of the two methods.

Various cardiac strains can be computed from the estimated displacement fields. In our work, the frame-to-frame displacements are further accumulated in time, to allow for the calculation of myocardial point trajectories. Indeed, from the estimated trajectories in time on two patients with infarcts, the shape of the trajectories of myocardial points belonging to pathological regions are clearly reduced in magnitude compared with the ones from normal regions. Myocardial point trajectories, estimated from our phase-based analytic signal approach, are therefore a good indicator of the local cardiac dynamics. Moreover, they are shown to be coherent with the estimated deformation of the myocardium.

Keywords: Motion estimation, Iterative bilinear model, Motion compensation, Phase invariance assumption, Analytic signal, Cardiac motion and strains, Local region tracking, Optical flow

1. Introduction

The mechanical status of the pathological heart can be assessed from the cardiac motion and strains evaluated in cardiac imaging. Among the different medical imaging modalities, echocardiography and cardiac magnetic resonance imaging (MRI) are the most widely used for cardiac motion estimation. In the technique of MR tagging, the cardiac tissue is marked with a grid of magnetically saturated tags; the deformation of the tags follows that of the myocardium during the cardiac cycle. To date, several methods have been proposed to estimate the motion from tagged MRI sequences (Axel and Dougherty, 1989) from prior semi-automatic tag pattern extraction (Guttman et al., 1994; O'Dell et al., 1995) and optical flow-based techniques (Prince and McVeigh, 1992). Spatial phase has been proposed as a measurement less prone to image intensity variations. Osman et al. introduced the harmonic phase (HARP) approach, which relies on the bandpass filtering of the tagged MR images in the Fourier domain (Osman et al., 1999; Dallal et al., 2012). In the SinMod approach introduced in (Arts et al., 2010), the intensity distribution in the environment of each pixel is modeled as a summation of sine wavefronts, obtained from tuned 2D bandpass filters. The method is fast and has shown better robustness to noise than the reference HARP method. Alternatively, a new method has been developed based on the temporal conservation of the monogenic phase (Alessandrini et al., 2013). In that work, a coarse-to-fine B-spline scheme allows for the effective and robust computation of the displacement, and also a pyramidal refinement scheme helps to deal with large motions. From the myocardial motion field, various further studies have been realized in order to extract motion-related information, such as myocardium segmentation (Dietenbeck et al., 2014), local deformation (Kar et al., 2014; Oubel et al., 2012), and local region tracking (Arif et al., 2014; Luo et al., 2014; Sun et al., 2011). For these information extraction methods, the key point is to estimate an accurate myocardium motion field.

The contributions of this paper are the following: We propose a two-dimensional (2D) phase-based motion estimation method. The estimated motion vectors are locally controlled by a bilinear transformation; the motion field between each two successive images is refined iteratively; the local non-rigid motion model and the global motion compensation model provide an accurate motion field estimation.

The proposed estimation algorithm is evaluated through several simulations. Both the Eulerian and Lagrangian displacement cases (Ricco and Tomasi, 2012) are discussed in the evaluation, which correspond, respectively, to two successive frame displacement and accumulated displacements (the points trajectory over time). The endpoint error (Fleet and Jepson, 1990) is used for Eulerian displacement evaluation. Additionally, from the Lagrangian motion field, we present the myocardium deformation and local region tracking results. The Green-Lagrange strain tensor (Belytschko et al., 2013) is used to calculate the radial and circumferential deformation (Petitjean et al., 2005). For two clinical cases with cardiac pathologies, the myocardium deformations and local region tracking results are presented and discussed.

The paper is organized as follows. Section 2 introduces the proposed 2D phase-based method. In section 3, the results are presented through the simulated and clinical image sequences. Section 4 concludes this paper and presents our perspectives.

2. Method

The proposed method estimates the displacement between two images. It is based on two spatial phase images, provided by 2D analytic signals of tagged MR images. Firstly, the procedure of spatial phase extraction is introduced. Next, we describe the mathematical development of the proposed displacement/velocity analytical estimator, which is applied on the phase images. Then, we show how the local complexity of cardiac motion is taken into account by a local bilinear model. Finally, an iterative scheme is presented to achieve subpixel motion accuracy.

2.1. Spatial phases from 2D analytic signal

The multidimensional extension of the 1D analytic signal (AS) can be found in the work on the 2D AS by Hahn (Hahn, 1992), the quaternion analytic signal (QS) of Bülow and Sommer (Bülow and Sommer, 2001), as well as the monogenic signal of Felsberg (Felsberg and Sommer, 2001). Multidimensional ASs have different forms but are all based on direct extensions of the 1D, 2D, or n-dimensional Hilbert transform. A phase-based method has been proposed by Basarab (Basarab et al., 2009) for the application of subsamples shift estimation on ultrasound images, which has stable accuracy for the low sampled signal.

Let us recall firstly the basic principles for calculating the 1D AS. Based on the Hilbert transform, Gabor in 1946 defined the AS of a 1D real signal (Gabor, 1946). An AS $s_A(x)$ of a real-value signal $f(x)$ contains two parts: a real part (the signal itself) and an imaginary part $f_H(x)$ (Hilbert transform of $f(x)$). $s_A(x)$ can be written as:

$$s_A(x) = f(x) + if_H(x) = f(x) + if(x) \star \frac{1}{\pi x}, \tag{1}$$

where i is the imaginary unit, and $\star$ denotes the convolution operator.

For a 2D real-value signal $f(x, y)$ with Cartesian coordinates (x, y), the total and the partial Hilbert transforms are, respectively, defined by (Hahn, 1992; Bülow and Sommer, 2001):

$$f_H(x, y) = f(x, y) \star\star (\frac{1}{\pi^2 xy}), \tag{2}$$

$$f_{H1}(x, y) = f(x, y) \star (\frac{1}{\pi x}), \tag{3}$$

$$f_{H2}(x, y) = f(x, y) \star (\frac{1}{\pi y}), \tag{4}$$

where $\star$ and $\star\star$ are the 1D and 2D convolution products, respectively. These three Hilbert transforms may be further combined to form the 2D QS and the 2D AS.

The 2D QS is defined as:

$$s_Q(x, y) = f(x, y) + if_{H1}(x, y) + jf_{H2}(x, y) + kf_H(x, y), \tag{5}$$

where i, j, k are the imaginary units with $ij = -ji = k, jk = -kj = i, ki = -ik = j$. Its polar form introduced by Bülow's definition is given in Eq. (6):

$$s_Q(x, y) = \left|s_Q(x, y)\right| e^{i\phi_i(x,y)} e^{k\phi_k(x,y)} e^{j\phi_j(x,y)}, \tag{6}$$

where $\left|s_Q(x, y)\right|$ is the modulus of $s_Q(x, y)$ and $(\phi_i(x, y), \phi_j(x, y), \phi_k(x, y))$ is called the phase of $s_Q(x, y)$.

The 2D AS is composed of four single-quadrant complex signals respectively given as a function of total and partial Hilbert transforms of $f(x, y)$ by (Hahn, 1992):

$$\begin{aligned} s_1(x, y) &= (f(x, y) - f_H(x, y)) + i(f_{H1}(x, y) + f_{H2}(x, y)) \\ &= |s_1(x, y)| e^{i\phi_1(x,y)}, \end{aligned} \tag{7}$$

$$\begin{aligned} s_2(x, y) &= (f(x, y) + f_H(x, y)) + i(-f_{H1}(x, y) + f_{H2}(x, y)) \\ &= |s_2(x, y)| e^{i\phi_2(x,y)}, \end{aligned} \tag{8}$$

$$\begin{aligned} s_3(x, y) &= (f(x, y) + f_H(x, y)) + i(f_{H1}(x, y) - f_{H2}(x, y)) \\ &= |s_3(x, y)| e^{i\phi_3(x,y)}, \end{aligned} \tag{9}$$

$$\begin{aligned} s_4(x, y) &= (f(x, y) - f_H(x, y)) + i(-f_{H1}(x, y) - f_{H2}(x, y)) \\ &= |s_4(x, y)| e^{i\phi_4(x,y)}, \end{aligned} \tag{10}$$

where i is the imaginary unit, $|s_1(x, y)|$, $|s_2(x, y)|$, $|s_3(x, y)|$, $|s_4(x, y)|$ are the modulus, and $\phi_1(x, y)$, $\phi_2(x, y)$, $\phi_3(x, y)$, $\phi_4(x, y)$ are the phases of $s_1(x, y)$, $s_2(x, y)$, $s_3(x, y)$, $s_4(x, y)$, respectively.

For our 2D motion estimation problem, we have locally two unknown variables to estimate, which are the displacement/velocity along the horizontal and vertical directions. Since it is known that the phase is less sensitive to global changes in the intensity of the image, in order to solve the 2D motion estimation problem, the information of two suitable phases should be chosen from the QS phases in Eq. (6) and AS phases in Eqs. (7)-(10). Due to the 2D spectrum symmetry of the 2D Fourier transform of real images, s_1 together with s_2 (or s_3 with s_4) contains all the information of the original image. Moreover, these two spatial phases contain complementary information about the image structure. For example, in the tagged MR image of Fig. 1, the tagging lines along two directions constitute two complementary structural information.

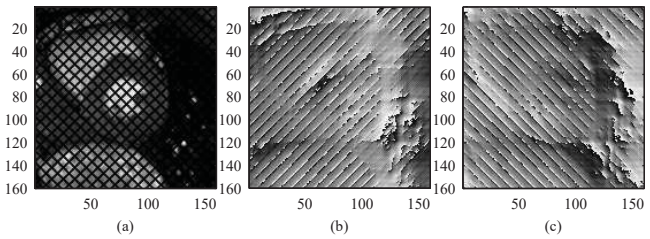

Figure 1: (a) Tagged MR image with 45° and 135° tagging lines. (b) Phase image ϕ_1 from analytic signal s_1, contains 45° tagging lines structural information. (c) Phase image ϕ_2 from analytic signal s_2, contains 135° tagging lines structural information.

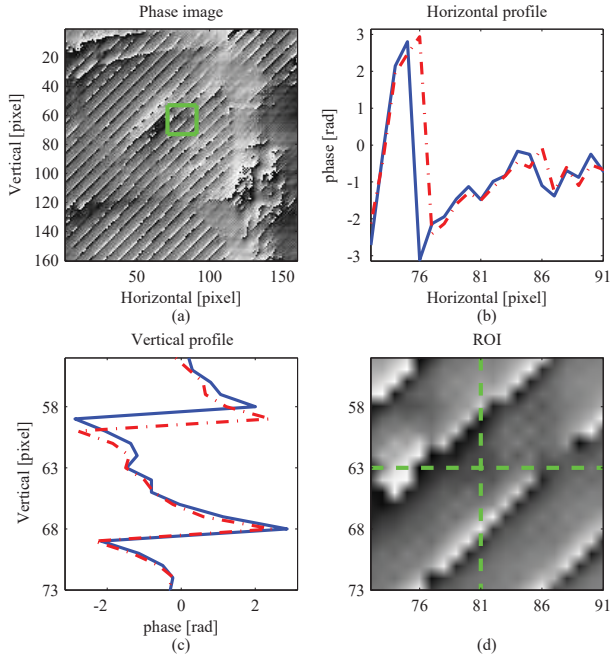

Figure 2: (a) Phase image ϕ_1 from analytic signal s_1 with an ROI in the green rectangle. (b) Horizontal profiles of two successive frames in ϕ_1 ROI in (d). (c) Vertical profile of two successive frames in ϕ_1 ROI in (d). (d) ROI (zoomed in) of ϕ_1 in (a) with horizontal/vertical profile lines (green dashed lines).

Although there exists a linear relation between the QS phases ϕ_i, ϕ_j and the AS phases $\phi_1, \phi_2, \phi_3, \phi_4$, while the QS phase ϕ_k contained the modulus of AS (Hahn and Snopek, 2004; Hahn, 2011), the QS phases do not split information in the two tagging line directions. This makes QS less suitable for calculating the spatial gradient of the phase needed in the next step of our method. Therefore, we use ϕ_1, ϕ_2 of s_1, s_2 in Eq. (7) and Eq. (8) as a basis for the myocardium displacement estimation in our method.

Figure 1 shows the spatial phases obtained via the AS s_1 and s_2, on a tagged MR image with tagging lines along the 45° and 135° directions. ϕ_1 holds the structural information of the 45° tagging lines, while ϕ_2 holds the ones of the 135° tagging lines. An example of the profile of phase ϕ_1 in a region of interest (ROI) of Fig. 1(b) is shown in Fig. 2.

2.2. Optical flow method from the spatial phase images

The optical flow equation is largely used for motion estimation in various application domains. It is based on the assumption of pixel intensity conservation over time, and of small displacements between consecutive frames (typically smaller than 1 pixel). Based on these hypothesis and using a Taylor series development of order 1, the optical flow equation is written as:

$$\begin{aligned} i(x,y,t) &= i(x+d_x, y+d_y, t+d_t) \\ &= i(x,y,t) + d_x\frac{\partial i}{\partial x} + d_y\frac{\partial i}{\partial y} + d_t\frac{\partial i}{\partial t} + O(d_x^2, d_y^2, d_t^2) \\ \Leftrightarrow & d_x\frac{\partial i}{\partial x} + d_y\frac{\partial i}{\partial y} + d_t\frac{\partial i}{\partial t} = 0, \end{aligned} \tag{11}$$

where i is the intensity function of space (x, y) and time (t) variables, d_x and d_y the displacement of the pixel at position (x, y), d_t the temporal sampling step, and $O(d_x^2, d_y^2, d_t^2)$ is the higher-order term. In the following, without loss of generality, we use $d_t = 1$ in order to simplify the mathematical expressions.

In this paper, we propose replacing the intensity invariance assumption by the phase over time. Thus, Eq. (11) is replaced hereafter by two equations holding on the two phases ϕ_1, ϕ_2 of AS s_1 and s_2:

$$d_x\frac{\partial\phi_1}{\partial x} + d_y\frac{\partial\phi_1}{\partial y} + \frac{\partial\phi_1}{\partial t} = 0, \quad d_x\frac{\partial\phi_2}{\partial x} + d_y\frac{\partial\phi_2}{\partial y} + \frac{\partial\phi_2}{\partial t} = 0. \tag{12}$$

Hence, dx, dy can be obtained by solving the previous system of two equations with two unknowns:

$$d_x = \frac{\frac{\partial\phi_1}{\partial y}\frac{\partial\phi_2}{\partial t} - \frac{\partial\phi_2}{\partial y}\frac{\partial\phi_1}{\partial t}}{\frac{\partial\phi_1}{\partial x}\frac{\partial\phi_2}{\partial y} - \frac{\partial\phi_1}{\partial y}\frac{\partial\phi_2}{\partial x}}, \quad d_y = \frac{\frac{\partial\phi_1}{\partial x}\frac{\partial\phi_2}{\partial t} - \frac{\partial\phi_2}{\partial x}\frac{\partial\phi_1}{\partial t}}{\frac{\partial\phi_1}{\partial y}\frac{\partial\phi_2}{\partial x} - \frac{\partial\phi_1}{\partial x}\frac{\partial\phi_2}{\partial y}}, \tag{13}$$

where $\frac{\partial\phi_1}{\partial x}$, $\frac{\partial\phi_2}{\partial x}$, $\frac{\partial\phi_1}{\partial y}$, $\frac{\partial\phi_2}{\partial y}$ are the spatial derivatives of ϕ_1 and ϕ_2 with respect to the spatial coordinates. The terms $\frac{\partial\phi_1}{\partial t}$ and $\frac{\partial\phi_2}{\partial t}$ are the temporal derivatives of the phases. They may be classically calculated by finite difference numerical differentiation. We propose, in order to avoid the phase jumps problem and possible errors of phase unwrapping, computing the temporal derivatives of the phases directly from the AS and its conjugates:

$$\frac{\partial\phi_1}{\partial t} = Arg[s_1^*(x,y,t)\cdot s_1(x,y,t+1)], \tag{14}$$

$$\frac{\partial\phi_2}{\partial t} = Arg[s_2^*(x,y,t)\cdot s_2(x,y,t+1)], \tag{15}$$

with s_1^* the conjugate of s_1, and s_2^* the conjugate of s_2. In the following, phases are computed using Eqs. (7) and (8) within local blocks extracted from tagged MR images and used to assess a local bilinear model.

2.3. Bilinear model of the local motion

Since the human myocardium has a relatively complex motion, the local displacement of myocardium cannot be estimated

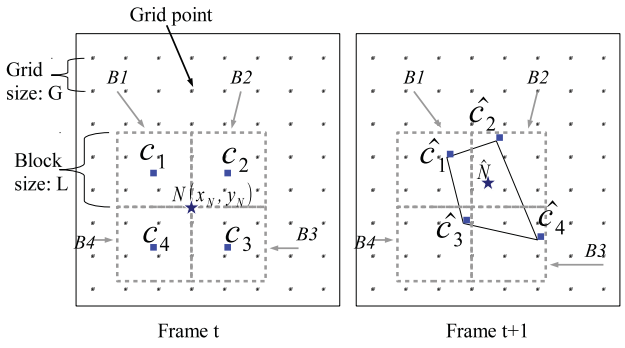

Figure 3: Displacement estimation between point $N(x_N, y_N)$ (star) on frame t and point $\hat{N}$ on frame t+1: Firstly, the displacement of four neighbor blocks $B1, B2, B3, B4$ of N are estimated separately, the average motion vector of each block is used as its center displacement from c_i to $\hat{c}_i$ (i=1,2,3,4). Next, the displacement of N to $\hat{N}$ is calculated by the bilinear model based on the position of $\hat{c_1}, \hat{c_2}, \hat{c_3}, \hat{c_4}$.

accurately by a simple rigid translation model. As a consequence, a more complex motion model is needed to approach local displacement better. In this paper, we used a bilinear model consisting of translation, dilation, rotation, and motion components. Such a model has already been used, for instance, for tissue displacement estimation in ultrasound elastographic image sequences (Basarab et al., 2008).

The basic principle is shown in Fig. 3. It illustrates how to calculate the displacement of the pixel $N(x_N, y_N)$ (star) between frame t and frame $t+1$. Let us define $B1, B2, B3, B4$ as the four blocks having in common the pixel N, and C_1, C_2, C_3, C_4 the centers of the blocks $B1, B2, B3, B4$. By applying Eqs. (7) and (8) on block Bi, we get its AS s_{1B}, s_{2B} and the phases ϕ_{1B}, ϕ_{2B}. Substituting into Eq. (13), we obtain the two displacement components $\left(d_x(C), d_y(C)\right)$:

$$d_x(C) = \frac{\frac{\partial\phi_{1B}}{\partial y}\frac{\partial\phi_{2B}}{\partial t} - \frac{\partial\phi_{2B}}{\partial y}\frac{\partial\phi_{1B}}{\partial t}}{\frac{\partial\phi_{1B}}{\partial x}\frac{\partial\phi_{2B}}{\partial y} - \frac{\partial\phi_{1B}}{\partial y}\frac{\partial\phi_{2B}}{\partial x}}, d_y(C) = \frac{\frac{\partial\phi_{1B}}{\partial x}\frac{\partial\phi_{2B}}{\partial t} - \frac{\partial\phi_{2B}}{\partial x}\frac{\partial\phi_{1B}}{\partial t}}{\frac{\partial\phi_{1B}}{\partial y}\frac{\partial\phi_{2B}}{\partial x} - \frac{\partial\phi_{1B}}{\partial x}\frac{\partial\phi_{2B}}{\partial y}}, \tag{16}$$

with $\frac{\partial\phi_{1B}}{\partial t} = Arg[s_{1B}(x,y,t) \cdot s^*_{1B}(x,y,t+1)]$, and $\frac{\partial\phi_{2B}}{\partial t} = Arg[s_{2B}(x,y,t) \cdot s^*_{2B}(x,y,t+1)]$. Therefore, we obtain the displacements $[d_x(C_1), d_y(C_1)]$, $[d_x(C_2), d_y(C_2)]$, $[d_x(C_3), d_y(C_3)]$, and $[d_x(C_4), d_y(C_4)]$ from blocks $B1$, $B2$, $B3$, and $B4$, respectively. The displacement $[d_x(N), d_y(N)]$ of grid point $N(x_N, y_N)$ can be calculated by the four displacements of point C_1, C_2, C_3, and C_4 as below. For this, the eight parameters of the bilinear model are estimated as follows:

$$\begin{pmatrix} a_x \\ b_x \\ c_x \\ d_x \end{pmatrix} = M \begin{pmatrix} d_x(C_1) \\ d_x(C_2) \\ d_x(C_3) \\ d_x(C_4) \end{pmatrix}, \begin{pmatrix} a_y \\ b_y \\ c_y \\ d_y \end{pmatrix} = M \begin{pmatrix} d_y(C_1) \\ d_y(C_2) \\ d_y(C_3) \\ d_y(C_4) \end{pmatrix}, \tag{17}$$

where the matrix M is depends on the block size L in Fig. 3:

$$M = \frac{1}{2}\begin{pmatrix} -\frac{1}{L} & \frac{1}{L} & \frac{1}{L} & -\frac{1}{L} \\ -\frac{1}{L} & -\frac{1}{L} & \frac{1}{L} & \frac{1}{L} \\ \frac{2}{L^2} & -\frac{2}{L^2} & \frac{2}{L^2} & -\frac{2}{L^2} \\ \frac{1}{2} & \frac{1}{2} & \frac{1}{2} & \frac{1}{2} \end{pmatrix}. \tag{18}$$

Then, the displacement of point $N(x_N, y_N)$ is obtained by:

$$\begin{aligned} d_x(N) &= a_x x_N + b_x y_N + c_x x_N y_N + d_x, \\ d_y(N) &= a_y x_N + b_y y_N + c_y x_N y_N + d_y. \end{aligned} \tag{19}$$

The detailed procedure is introduced in (Basarab et al., 2008). Finally, the dense motion field is calculated by linear interpolation from the displacement of the grid points. In order to improve the estimation accuracy, a global refining method is proposed in the following.

2.4. Refined model

For two successive images i_t and i_{t+1}, an initial estimation of the displacement field (d^0_x, d^0_y) is obtained as described in the previous section:

$$\left[d^0_x(x,y), d^0_y(x,y)\right] = \Delta\left[i_t(x,y), i_{t+1}(x,y)\right], \tag{20}$$

where Δ is the motion estimator described in section 2.3. Based on this motion field and the first image $i_t(x,y)$, an inter-frame $\hat{i}^1_{t+1}(x,y)$ is generated by:

$$\hat{i}^1_{t+1}(x,y) = i_t\left(x + d^0_x(x,y), y + d^0_y(x,y)\right), \tag{21}$$

where the new position of the pixel (x_0, y_0) in $i_t(x,y)$ is $[x_0 + d^0_x(x_0,y_0), y_0 + d^0_y(x_0,y_0)]$ and each pixel value of $\hat{i}^1_{t+1}(x,y)$ is obtained by spline interpolation.

Ideally, the generated image $\hat{i}^1_{t+1}(x,y)$ and the image $i_{t+1}(x,y)$ should contain the same phase information. However, in practice, this is not true because of motion estimation errors. Therefore, a compensated motion field $[d^1_{xc}(x,y), d^1_{yc}(x,y)]$ is estimated between image $\hat{i}^1_{t+1}(x,y)$ and $i_{t+1}(x,y)$ by the same bilinear phase-based optical flow method proposed in section 2.3:

$$\left[d^1_{xc}(x,y), d^1_{yc}(x,y)\right] = \Delta\left[\hat{i}^1_{t+1}(x,y), i_{t+1}(x,y)\right]. \tag{22}$$

Then, the estimated motion field $[d_x(x,y), d_y(x,y)]$ between two successive images i_t and i_{t+1} with improved accuracy is obtained by:

$$\begin{aligned} d_x(x,y) &= d^0_x(x,y) + d^1_{xc}(x,y), \\ d_y(x,y) &= d^0_y(x,y) + d^1_{yc}(x,y). \end{aligned} \tag{23}$$

This process can be iterated a number of times leading to the iterative scheme:

$$\begin{aligned} d^k_x(x,y) &= d^{k-1}_x(x,y) + d^k_{xc}(x,y), \\ d^k_y(x,y) &= d^{k-1}_y(x,y) + d^k_{yc}(x,y), \end{aligned} \tag{24}$$

with k the iteration number ($k \geqslant 1$). This iteration procedure is part of step 2 of Algorithm 1. (see section 2.5). With this iterative scheme, a more accurate motion field $[d_x(x,y), d_y(x,y)]$ is obtained.

2.5. Algorithm implementation

The pseudo-code of the proposed motion estimation method between two consecutive images is given in Algorithm 1.

Algorithm 1 Phase-based Bilinear block and Compensation Optical Flow

Input: two subsequent frames: $i_t(x, y), i_{t+1}(x, y)$.
parameter: G, L, kMax.
G: Gird distance for bilinear model in pixels on horizontal and vertical direction.
L: Block size for bilinear model in pixels on horizontal and vertical direction.
kMax: Maximum iteration number.

Output: Displacement $[d_x(x, y), d_y(x, y)]$ between $i_t(x, y)$ and $i_{t+1}(x, y)$.

Step 1:
for (x, y) = grid points coordinate on frame i_t **do**
  for each of the four neighbour block of the current grid point **do**
    $[s_{1B}(t), s_{2B}(t), \phi_{1B}(t), \phi_{2B}(t)]$ = BlockAS($B(t)$).
    $[s_{1B}(t+1), s_{2B}(t+1), \phi_{1B}(t+1), \phi_{2B}(t+1)]$ = BlockAS($B(t+1)$).
    {Eqs. (7),(8).}
    $\left[d_x(C), d_y(C)\right]$ = PhaseOpticalFlow($s_{1B}, s_{2B}, \phi_{1B}, \phi_{2B}$).
    {Eq. (16).}
  end for
  $[d_x(N), d_y(N)]$=BilinearModel($[d_x(\mathbf{C}), d_y(\mathbf{C})]$).
  {Compute the displacement of the current grid point N.}
end for
$\left[d_x^0(x, y), d_y^0(x, y)\right]$=DenseMotion($[d_x(N), d_y(N)]$).
{Interpolation on all the grid point N to obtain dense motion field}
Step 2:
$d_x^{k-1}(x, y) = d_x^0(x, y), d_y^{k-1}(x, y) = d_y^0(x, y)$
{initialize for refining interation k.}
for k=1:$kMax$ **do**
  {$kMax$ is the maximum iteration number}
  $\hat{i}_{t+1}^k$=ObjectFrameGeneration($d_x^{k-1}, d_y^{k-1}, i_t$). {Eq. (21).}
  $[d_{xc}^k, d_{yc}^k]$=CompensatedDisplacement($\hat{i}_{t+1}^k, i_{t+1}$).
  {Repeat **Step 1** by Eq. (22).}
  $d_x^k = d_x^{k-1} + d_{xc}^k, d_y^k = d_y^{k-1} + d_{yc}^k$ {Eq. (23).}
end for
$d_x(x, y) = d_x^{kMax}(x, y), d_y(x, y) = d_y^{kMax}(x, y)$

3. Results

The proposed method was evaluated on both synthetic and clinical data.

3.1. Simulated data

The proposed method was tested on different realistic tagged MRI sequences corresponding to a cardiac cycle, simulated with ASSESS software (Clarysse et al., 2011). With this simulator, a combination of thickening and rotations simulates the contraction over time within a short-axis MRI slice. It is also possible to introduce a local motion anomaly by reducing the myocardium contraction magnitude within a myocardial sector (Clarysse et al., 2000). Therefore, the ground truth motion data were used as a reference to evaluate the proposed method. Several simulations were generated by acting on the simulator parameters. Each simulation term in Table 1 can be interpreted as follows: "256" or "160" for the resolution of each square frame in pixels, "D20" for contraction/expansion of 20%, "R20" for 20-degree rotation, "F20" or "F34" for frame number of 20 or 34, and "P0" for healthy or "P3" for pathological state with the highest degree of the myocardial motion abnormality.

3.2. Robustness of phase

In order to evaluate the robustness of our method, we also generated a sequence imposing a non respect of the pixel intensity conservation over time, named "160D30R20P3F34Lum" in Table 1. In each image of the sequence, we changed its intensity by a random percentage value between 40% and 100% of the original intensity. In order to modify the intensity of each image of the sequence, we multiplied the original image by a 2D weighting image $(a + (1 - a)G(x, y))$, with $G(x, y)$ the Gaussian function. The range of the 2D weighting image is $(a, 1]$, where a is a random real value limited in $[0.4, 1]$. As the consequence, we obtain a sequence with the pixel intensity of 40% and 100% of the original image intensity. Here we chose the minimum value $a = 0.4$ for the purpose of retaining at least 40% intensity of the original images.

The sequence intensity changes locally in each frame due to the Gaussian function and also changes along the time axis due to the random value a. Given an original image i_1, the output image i_2 obtained by the 2D weighting image $(a+(1-a)G(x, y))$ is:

$$i_2(x, y) = (a + (1 - a)G(x, y))i_1(x, y), \tag{25}$$

where $G(x, y) = exp\left(-\frac{(x-x_0)^2+(y-y_0)^2}{2\sigma^2}\right)$, with (x_0, y_0) and σ the center peak position and the standard deviation of $G(x, y)$, respectively. We vary the center peak position (x_0, y_0) linearly along the time axis, which changes the brightest region on each frame in the sequence. Figure 4 shows an example: each pixel value of the image in Fig. 4(b) is obtained from the corresponding pixel value of image in Fig. 4(a) multiplied by the corresponding value of 2D weighting image in Fig. 4(e). Figures 4(c) and (d) are one of the phases of Fig. 4(a) and (b), respectively. We note that both phase images hold the structural information and are less influenced by their varied intensity images.

3.3. Existing methods used for comparison

Taking into account the fact that the proposed method is based on the analytic signal and optical flow principles (more precisely on the phase flow), the evaluation results of an analytic signal estimator and optical flow estimator are presented for comparison purposes.

The first one is the Alessandrini monogenic signal method for the analysis of heart motion from medical images (Alessandrini et al., 2013). It outperforms the SinMod method (Arts et al., 2010) and was shown to be more accurate with less computation than another algorithm based on the monogenic signal (Zang et al., 2007).

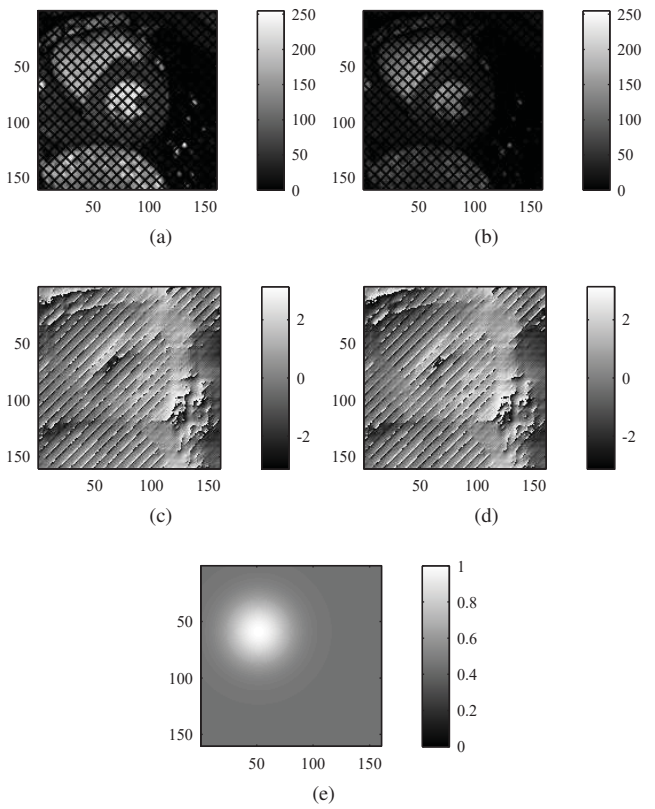

Figure 4: (a) A tagged MR image. (b) Modified intensity image of (a) by weighting image (e). (c) The phase of (a). (d) The phase of (b). (e) 2D weighting image from the Gaussian function($\sigma = 20$, $(x_0, y_0) = (59, 52)$, $a = 0.45$). The phase images (c) and (d) contain almost the same structural information as the different intensity image (a) and (b).

The second method used for comparison is called Sun classic NL in (Sun et al., 2010). It was declared the best optical flow algorithm in 2010 in the Middlebury evaluation ranking (Baker et al., 2007, 2011) (used for the evaluation of optical flow algorithms), and in an expanded literature review in 2014 (Sun et al., 2014). This method was also reported to provide good results in the new optical evaluation datasets in 2012 such as KITTI (Geiger et al., 2012) (autonomous driving platform to develop new benchmarks for the tasks of stereo, optical flow, and 3D object detection) and MPI Sintel (Butler et al., 2012) (new optical flow data set derived from the open source 3D animated short film Sintel). Hence, these two algorithms could be considered as suitable references.

3.4. Evaluation criteria

Angular error (AE) and endpoint error (EE) are common criteria used to evaluate the difference between the theoretical and estimated displacements. However, AE is less suitable for small displacements (Alessandrini et al., 2013) and the EE is a more appropriate measure of displacement vector accuracy (Baker et al., 2011). Hence, we used EE to evaluate the estimation accuracy. The EE at one location is defined as:

$$EE(x,y) = \sqrt{(d_x(x,y) - d_{xr}(x,y))^2 + (d_y(x,y) - d_{yr}(x,y))^2}, \tag{26}$$

where $\left[d_{xr}(x,y), d_{yr}(x,y)\right]$ are the ground truth reference displacements along horizontal and vertical directions, respectively, and $\left[d_x(x,y), d_y(x,y)\right]$ are the estimated ones. The averages and standard deviations of EE for both Eulerian and Lagrangian displacements are computed to quantify the performance of the method. The EE values obtained for several simulation sequences results are presented and discussed in the following sections.

3.5. Method parameters

The parameters for all the methods are determined based on the sequences in Table 1. With the proposed method, for the bilinear model, the grid distance is 4×4 pixels and the block size is 10×10 pixels. Two refinement iterations appear as a good trade-off between EE and computing time. We computed the motion field for all the seven simulated sequences, then obtained an average of these seven sequences' EE, which equals 0.055,0.042,0.039,0.037 pixels, receptively, corresponding to iteration number 1,2,3,4.

Moreover, the computing time to finish calculating all the seven sequences (80 images of 256×256 pixels and 102 images of 160×160 pixels) is 18.59, 27.87, 37,18, 46.54 minutes, receptively, corresponding to the iteration number 1,2,3,4. With Alessandrini method, the optimized parameters proposed in (Alessandrini et al., 2013) are used, which are the initial wavelength $\lambda_0 = 4$ and the refinement step number $N_p = 5$. For the Sun classicNL method, we adopted the parameters recommended in (Sun et al., 2010), which are the sobel edge detector with a mask of 5×5 pixels and a neighborhood of 15×15 pixels.

3.6. Eulerian motion estimation results

3.6.1. Global results for all simulation sequences

Table 1 shows the EE results for the seven simulated sequences. For each sequence, we calculate a spatial average EE value μ and the standard deviation σ.

All the methods were implemented in MATLAB (R2012b, The Math-Works, Natick, MA), on a laptop computer (CPU: Intel i7-4750HQ 2.0GHz, RAM: 16384MB). Table 1 shows our results compared with the Alessandrini and Sun classicNL methods. Based on the summation of EE results of the seven sequences, the errors of the proposed method are reduced by 33% and 35% compared with that of the Alessandrini's and Sun's methods, respectively. On the variable intensity sequence "160D30R20P3F34Lum" and the constant intensity sequence "160D30R20P3F34," the proposed method provides a robust estimation. Besides, the proposed method is about 28% faster that Sun's method while providing a better motion estimation result. Although the Alessandrini method is outperformed by the proposed method, it is less time-consuming than the two other approaches.

	Endpoint Error [pixels]			Computing time [minutes]		
Sequence	Proposed	Alessandrini	Sun ClassicNL	Proposed	Alessandrini	Sun ClassicNL
(1)256R20F20	**0.050±0.055**	0.087±0.064	0.089±0.082	5.00	0.48	15.95
(2)256D30F20	**0.015±0.013**	0.035±0.025	0.036±0.034	5.00	0.52	13.43
(3)256D30R20P0F20	**0.063±0.066**	0.094±0.069	0.092±0.090	5.02	0.70	16.08
(4)256D30R20P3F20	**0.062±0.065**	0.099±0.075	0.097±0.095	5.02	0.68	16.03
(5)160D30R20P0F34	**0.035±0.027**	0.045±0.025	0.048±0.038	2.68	0.57	13.10
(6)160D30R20P3F34	**0.034±0.025**	0.041±0.022	0.045±0.035	2.58	0.58	13.52
(7)160D30R20P3F34Lum	**0.037±0.026**	0.042±0.022	0.049±0.037	2.57	0.58	14.73

Table 1: Eulerian average endpoint error ($\mu \pm \sigma$) in pixels on seven simulated sequences and their computing time

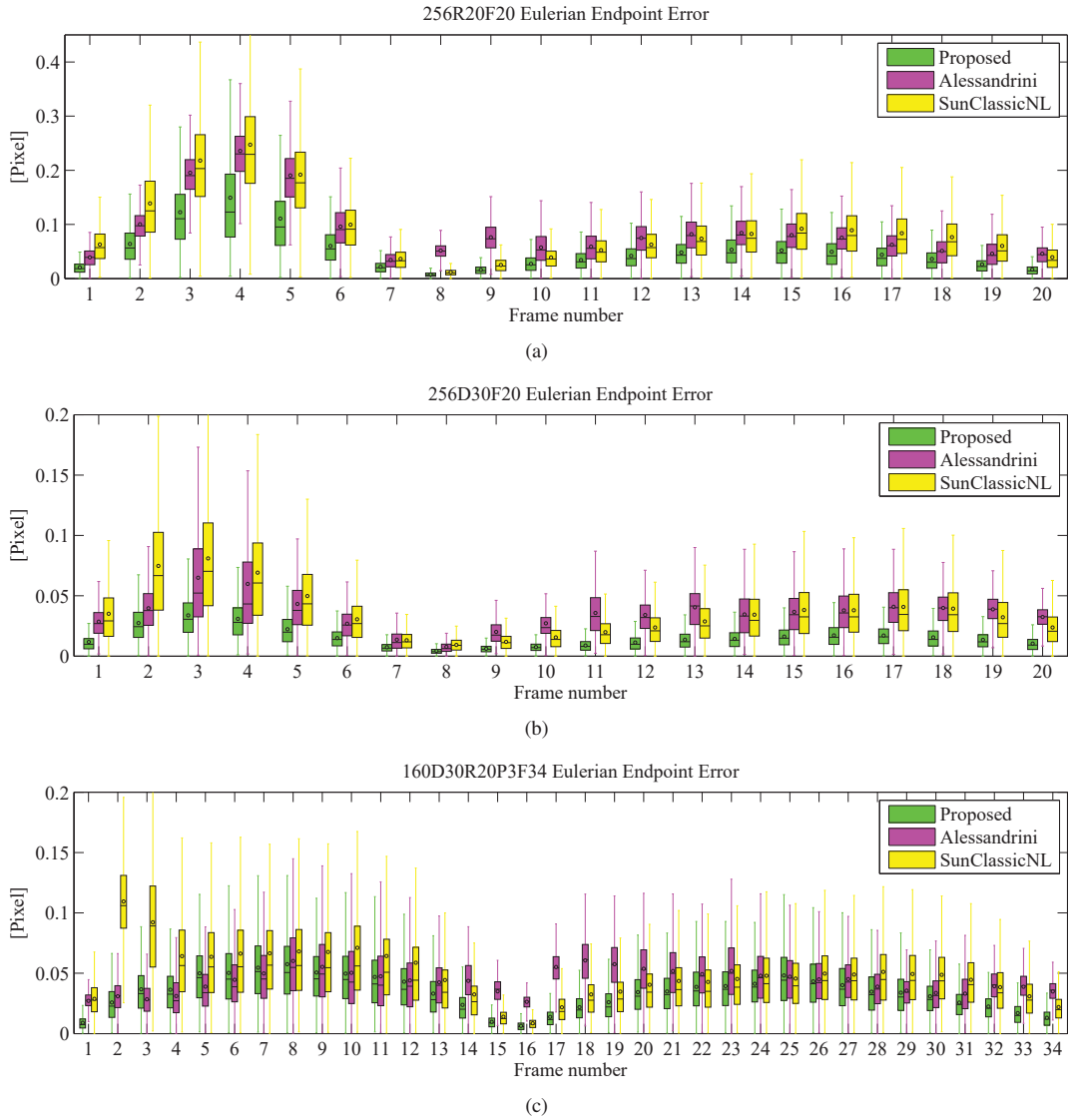

Figure 5: Box and whiskers plots of Eulerian endpoint errors for sequences (a) "256R20F20", (b) "256D30F20", (c) "160D30R20P3F34." Each box corresponds to the statistical distribution of all EE values on one frame. The center bar of each box represents the median value. The circle indicates the average value, and the box body extends from the 25th to the 75th percentile of one frame of EE values.

Figure 5 presents a frame-by-frame EE comparison through box and whiskers plots for three sequences. These sequences present different kinds of motions: pure rotation of sequence "256R20F20", pure contraction/expansion of sequence "256D30F20", and rotation+contraction/expansion+deformation of sequence "160D30R20P3F34". The sequences "256R20F20" and "256D30F20" contain 7 frames in the systolic and 13 frames

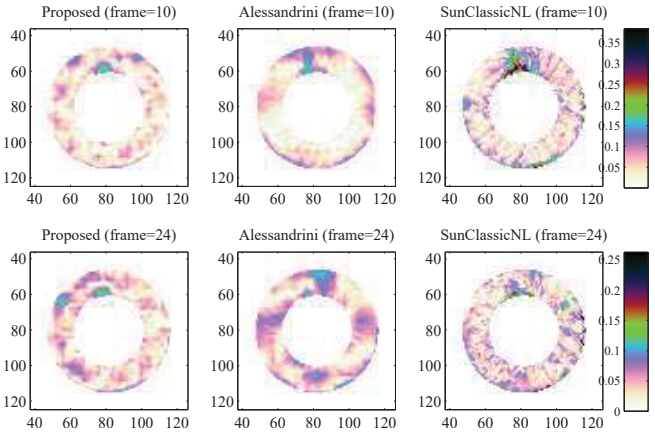

Figure 6: EE results of three methods (unit: pixels). First row: systolic frame 10. Second row: diastolic frame 24. First column: proposed method. Second column: Alessandrini method. Third column: Sun classicNL method.

in the diastolic phase of one cardiac cycle. The sequence "160D30R20P3F34" contains 14 and 20 frames in the systolic and diastolic phase, respectively.

In Fig.5(a) and Fig.5(b), it is clear that during the systolic phase (frame 1 to 7), which corresponds to the larger displacements and also the diastole phase (frame 8 to 20). The estimation results of the proposed method are much better than the other two methods. We obtain the smallest end point error on each frame from the proposed method. In Fig.5(c), during the systolic phase (frame 1 to 14), we obtain better estimation results with the proposed method than with the Sun classicNL method and almost equivalent estimation results as the Alessandrini method. At the beginning of the diastolic phase, the proposed method provides similar performance as the Sun classicNL method. In the diastole (frame 16 to 34), the proposed method is more accurate than the other two methods. Especially, in the frames where the displacement is relatively small, the proposed method outperforms the Alessandrini method at the frames 16 to 23, and it also outperforms the Sun classicNL method at frames 27 to 34.

3.6.2. Detailed EE results from one test case sequence

Performances of the three methods were studied in details on sequence "160D30R20P3F34", which presents one cardiac cycle represented by 14 frames in the systolic and 20 frames in the diastolic phase. Figure 6 compares the EE results between the three methods on a systolic frame and a diastolic frame. In the systolic frame result (first row), the proposed method generates smaller error values. In the diastolic frame result (second row), there is no very clear observable difference between the three methods.

To better understand the performance of the methods, it is important to analyze vertical and horizontal displacement separately. Accordingly, Fig. 7 presents these results at frame 10, which has one of the largest displacements of two successive frames during the cardiac cycle. The ground truth motions are in the first row; the proposed method results, Alessandrini results, and Sun classicNL results are displayed in the second,

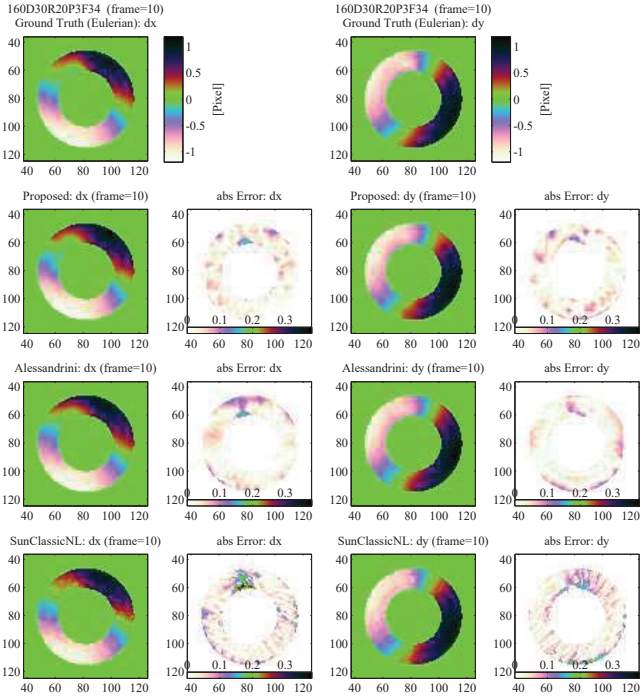

Figure 7: Displacement and absolute value error map in pixels of sequence "160D30R20P3F34" for three motion estimation methods. The horizontal displacement in pixels and its error are in the first column and second column, respectively. The vertical displacement in pixels and its absolute error are in the third and fourth columns, respectively. First row: the ground truth. Second row: the proposed method. Third row: Alessandrini method. Fourth row: Sun classicNL method.

third and fourth rows, respectively. d_x indicates the horizontal displacement (first column) with its absolute error map beside (second column). d_y represents the vertical displacement (third column) with its absolute error map on the right (fourth column). The comparison of the absolute error in the second and third row highlights that the EE map is slightly smaller in magnitude for our method as compared to the Alessandrini method. Also, the proposed method error is much smoother than the Sun classicNL method error.

Figure 8 presents frames 10 and 24 extracted from sequence "160D30R20P3F34" of one cardiac cycle with a superposition of the Eulerian motion vector estimated within the frames 10-11 and 24-25. The frames 10 and 24 belong, respectively, to systole and diastole phases, with a corresponding cardiac time in terms of the percentage value of one cardiac cycle period. These motion vectors vary for each frame, thus allowing for a local observation of the movement within the myocardium.

3.7. Lagrangian motion estimation results

The Lagrangian motion field represents the spatial displacement of material points in the reference state (first frame) along time. This spatio-temporal Lagrangian displacement field $[u_L(x,y), v_L(x,y)]$ can be recovered through forward integration of the Eulerian motion field $[d_x(x,y), d_y(x,y)]$. For a motion field between time t and $t+1$, we calculate the Lagrangian motion field $[u_L(x,y,t+1), v_L(x,y,t+1)]$ from the Lagrangian mo-

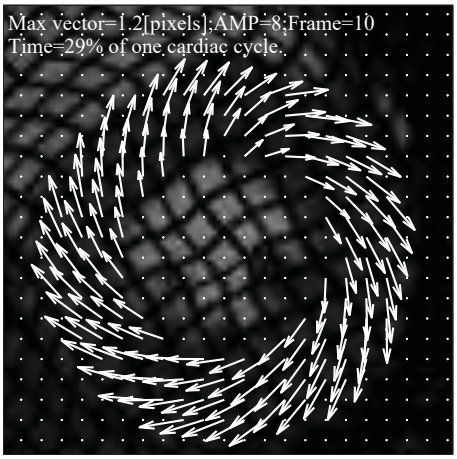

(a)

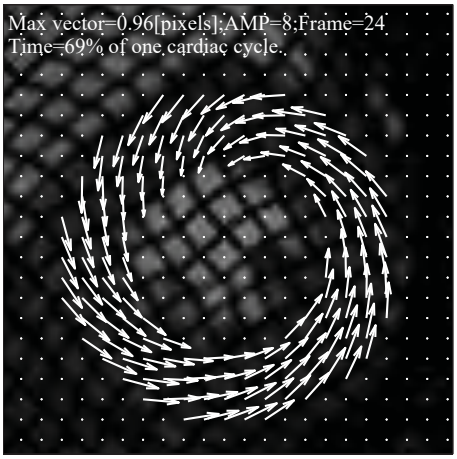

(b)

Figure 8: The Eulerian estimated motion vectors of sequence "160D30R20P3F34" from the proposed method. (a) Frames 10 from systole. (b) Frame 24 from diastole. Motion vectors are amplified by a factor of 8. The cardiac time of each frame is presented in terms of the percentage of a whole cardiac cycle.

tion field $[u_L(x, y, t), v_L(x, y, t)]$ at time t and the Eulerian motion field $[d_x(x, y, t + 1), d_y(x, y, t + 1))]$ at time $t + 1$:

$$u_L(x, y, t + 1) = u_L\Big(x + d_x(x, y, t + 1), y + d_y(x, y, t + 1), t\Big), \tag{27}$$

$$v_L(x, y, t + 1) = v_L\Big(x + d_x(x, y, t + 1), y + d_y(x, y, t + 1), t\Big), \tag{28}$$

with the initial conditions $u_L(x, y, 1) = d_x(x, y, 1)$, $v_L(x, y, 1) = d_y(x, y, 1)$. A bilinear interpolation is applied on the four neighbour points of the current point to calculate the motion field $u_L(x + d_x(x, y, t + 1), y + d_y(x, y, t + 1), t)$ and $v_L(x + d_x(x, y, t + 1), y + d_y(x, y, t + 1), t)$.

One major indicator for cardiac function diagnosis is represented by the myocardial strains (Qian et al., 2011), which can be computed from spatial derivatives of the Lagrangian accumulated motion field $\mathbf{u} = [u_L(x, y, t), v_L(x, y, t)]$ with respect to

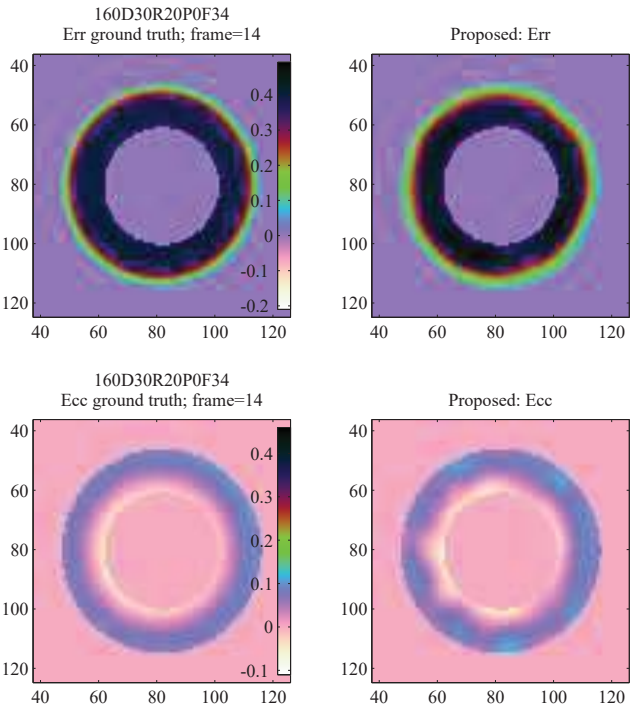

Figure 9: Estimated systolic myocardial strains in healthy case sequence. First row: radial deformation E_{rr}. Second row: circumferential deformation E_{cc}. First column: the ground truth. Second column: the proposed method results.

time. The Green-Lagrange strain tensor is defined as:

$$\mathbf{E} = \frac{1}{2}\left(\nabla\mathbf{u} + \nabla\mathbf{u}^T + \nabla\mathbf{u}^T\nabla\mathbf{u}\right), \tag{29}$$

where ∇ is the spatial derivative operator and $\mathbf{u}^T$ is the transpose of $\mathbf{u}$. Furthermore, the radial deformation E_{rr} along direction $\mathbf{r}$ and circumferential deformation E_{cc} along direction $\mathbf{c}$ can be obtained by:

$$E_{rr} = \mathbf{r}^T\mathbf{E}\mathbf{r}, \quad E_{cc} = \mathbf{c}^T\mathbf{E}\mathbf{c}. \tag{30}$$

In the simulated sequences "160D30R20P0F34" and "160D30R20P3F34," the systolic (from frame 1 to end-systolic frame 14) radial and circumferential strains were computed. Figure 9 shows the myocardial deformation at frame 14 of sequence "160D30R20P0F34." The uniformity of deformation is observable in this healthy case from both the ground truth and proposed method results.

Figure 10 shows the radial and circumferential strains for the pathological case (sequence "160D30R20P0F34"). The four columns are in the order of the ground truth, the proposed method result, the Alessandrini result, and the Sun classicNL result. A simulated pathology region is located in the upper left region of the myocardium (indicated by an arrow in the figure). From the radial deformation results E_{rr}, all three methods can recover the pathology, while from the circumferential deformation results, our proposed method obtains a more accurate pathology location than the other two methods.

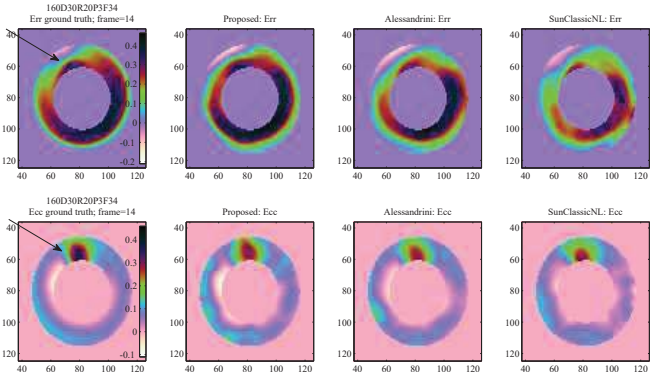

Figure 10: Estimated systolic myocardial strains for the pathological case sequence "160D30R20P3F34". First row: radial deformation E_{rr}. Second row: circumferential deformation E_{cc}. The four columns are in the order of the ground truth, the proposed method result, Alessandrini result, and Sun classicNL result, receptively.

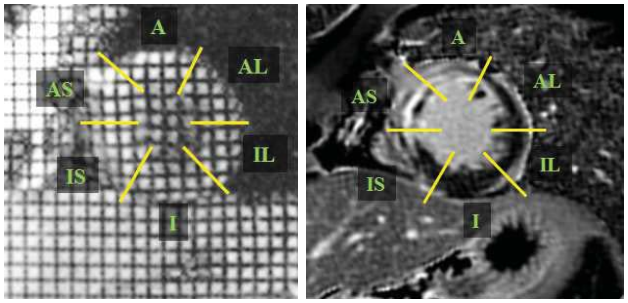

(a) (b)

Figure 11: Selected images of patient #1. (a) Short-axis tagged MR image. Frame 1 (end-diastolic phase) of this sequence that was used to estimate the motion field. (b) Image of LGE sequence with an area (edema in hypersignal) in the A, AS, and IS segments. A indicates anterior; AS, anteroseptal; IS, inferoseptal; I, inferior; IL, inferolateral; AL, anterolateral.

3.8. Clinical results

In this section, we applied our method to in vivo clinical sequences of pathological cases from a female patient (43 years old) and a male patient (65 years old).

3.8.1. Pathological case #1

This 43 year-old female acute myocardial infarction (AMI) patient was hospitalized with a left anterior descending (LAD) occlusion, with a reperfusion performed H+2. MR imaging was performed 5 days after reperfusion. The standard cardiovascular magnetic resonance (CMR) examination contained MR tagging and post-Gadolinium injection (10 minutes) with a 3D inversion-recovery gradient echo sequence. MR tagging was performed on a Siemens Avento 1.5T in short-axis and long-axis views with the following parameters: gradient echo (GRE) sequence with 45° spatial modulation of magnetization (SPAMM) tagging pattern, TE=1.39 *ms*, TR=26.4 *ms*, flip angle=20°, tag spacing=6 *mm*, spatial resolution=1×1 *mm*, 21 frames, temporal resolution=30 *ms*.

Figure 11(a) shows the first frame (end-diastolic phase) of a short-axis tagged slice located between the mid and apical level of the left ventricle. The myocardium is divided following the American Heart Association (AHA) segmentation (Cerqueira et al., 2002). Figure 11(b) shows the Late Gadolinium Enhancement (LGE) image at the same slice level. AMI appears as hyper-enhanced regions (AS, A, and IS segments) with dark regions in the sub-endocardial layers corresponding to no-reflow regions.

Applying the proposed method to this clinical tagged MRI sequence, the Lagrangian motion field is obtained by accumulating the Eulerian motion field. Figure 12 represents the Lagrangian motion field and the radial deformation (E_{rr}) at frame 13 (end-systole, corresponding to the maximum contraction). In Fig. 12(a), the amplitude of the movement in the A, AS, and IS segments are visibly smaller than in the AL, IL, and I segments, which is obviously in concordance with the location of the pathology. Due to the myocardial thickening during systole, radial strain is usually positive in normal myocardium. Figure 12(b) shows the reduced, and even negative, E_{rr} values in the pathological anterior region.

Lagrangian material point trajectories are displayed in Fig. 13. They provide a visual experience of the myocardium local motion trace. Several locations are chosen on the first image of the sequence as the desired tracking points. From the short-axis image in Fig. 13(a), we highlight clearly that during the cardiac cycle, the AS segment has decreased motion than other segments in adjacent or remote myocardium. In addition, in long-axis view shown in Fig. 13(b), we also illustrate a decrease of motion in the anteroapical, apical and infer-apical segments (in the white dashed circle). The white line shows the cross-location of the short axis view in Fig. 13(a). Hence, these tracking results are able to give an alternative illustration of the pathologies.

3.8.2. Pathological case #2

This second clinical case illustrates an inferior AMI in a 65 year-old male (right coronary occlusion - reperfusion H+5). Imaging was performed before discharge of the patient at day 5. A short-axis tagged MRI was performed on a Siemens Avento 1.5T with the following parameters: GRE sequence with 45° SPAMM tagging pattern, TE=1.53 *ms*, TR=36.4 *ms*, flip angle=20°, tag spacing=6 *mm*, spatial resolution=1×1 *mm*, 21 frames, temporal resolution=36.4 *ms*.

Figure 14(a) shows the end-diastolic frame of the short-axis tagged MR sequence at the mid level of the left ventricle. Figure 14(b) shows the LGE image at the same slice level as the tagged image in Fig. 14(a). Abnormal segments corresponding to myocardial necrosis are including the IS, I, and IL segments, with again, presence of no-reflow (sub-endocardial hyposignal) in the I and IL segments.

The estimated end-systolic motion field in Fig. 15(a) shows that the myocardium is almost divided in two parts: the upper one (anterior) with a centripetal movement of normal amplitude, and the inferior wall with a major decrease of amplitude. The radial strain map in Fig. 15(b) illustrates also the contrast between anterior and inferior parts of the circumference of the

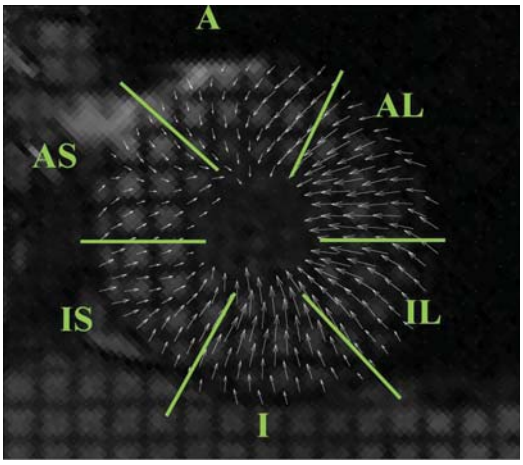

(a)

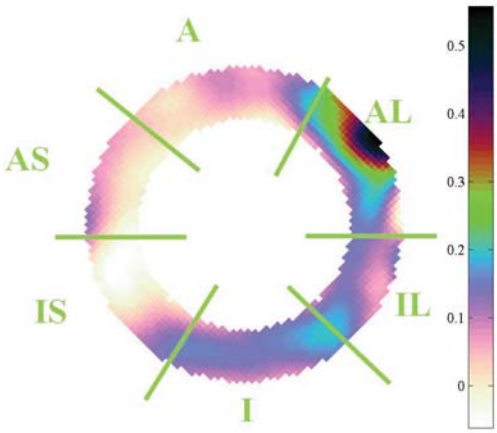

(b)

Figure 12: (a) Lagrangian motion field at end-systole frame 13 (with 1.5 magnification factor). (b) Radial strain E_{rr} at end-systole. The white regions (with reduced and negative values) in the A, AS and IS segments are matching the location of infarcted segments.

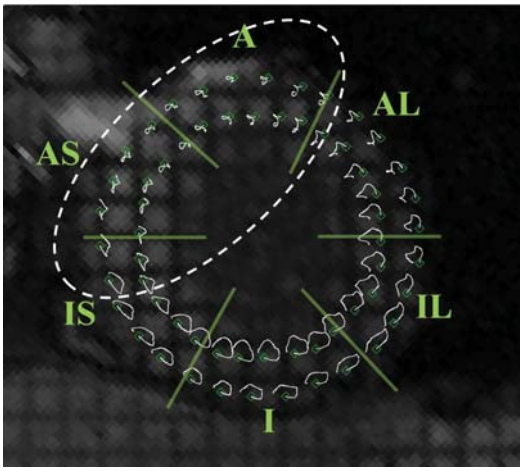

(a)

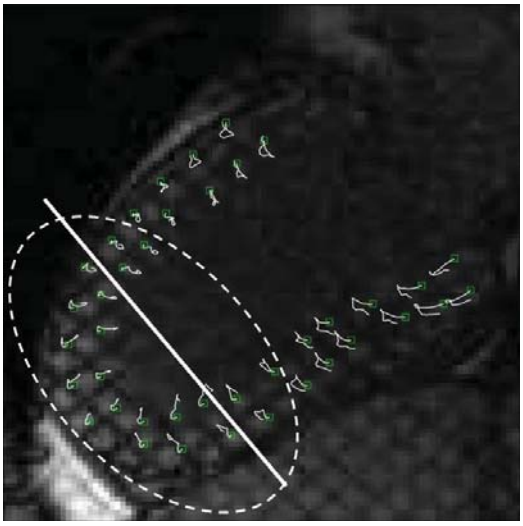

(b)

Figure 13: MR tagging-based material point trajectories for patient #1. (a) Short-axis view, note the reduced magnitude of motion in infarcted regions in the white dashed circle as compared to adjacent and remote regions. (b) Long-axis view, a white line indicates the position of the short axis plane in (a). The white dashed circle delineates the regions with decreased motion in this antero-septo-apical infarction.

myocardium. In the IS, I, and IL segments, most of the negative deformation values and small positive values can be found in the lower part of the myocardium.

The Lagrangian material point trajectories in Fig. 16(a) give a global view of the whole sequence along time. In the remote anterior regions A and AL segments (mostly), traces are smooth and large in amplitude. In the abnormal segments delineated with the dashed circle, traces are twisted and short, which demonstrate the lack of contractile capabilities in this acutely infarcted regions. In order to better highlight the difference between the healthy and pathological myocardial region tracking results, Fig. 16(b) presents the tracking results of a healthy myocardium from a male volunteer. We can see from this healthy case that all the tracked points have uniform contraction and dilation motions, which are different from the motion behavior of the pathological cases.

4. Conclusion

We have proposed in this paper a motion estimation method for tagged MRI sequences based on the 2D single quadrant AS phases and optical flow method. In the proposed method, the local bilinear model and a global refining method are employed on the optical flow motion field, improving the accuracy of displacement estimation in tagged MRI myocardium sequences. The performance of the proposed method is evaluated in several types of simulated sequences. Compared with two other effective methods (Alessandrini and Sun classicNL), the proposed method leads to a notable reduction of estimation errors. Moreover, the proposed method is less sensitive to both the pixel intensity variation over time and weak contrast sequences. These two phenomena typically occur in real clinical situations.

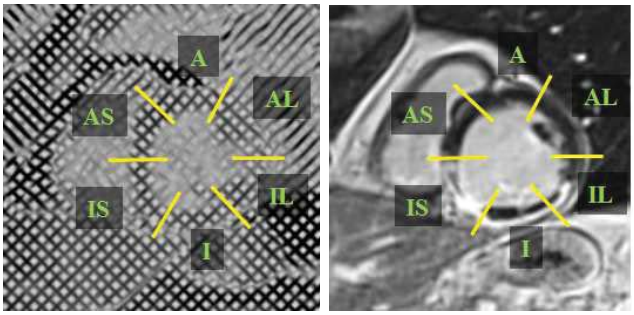

(a) (b)

Figure 14: Selected images of patient #2. (a) Short-axis tagged MR image. Frame 1 (end-diastolic phase) of this sequence that was used to estimate the motion field. (b) Corresponding slice of the LGE sequence showing an inferior infarction (hyper-enhanced regions) with no-reflow segments.

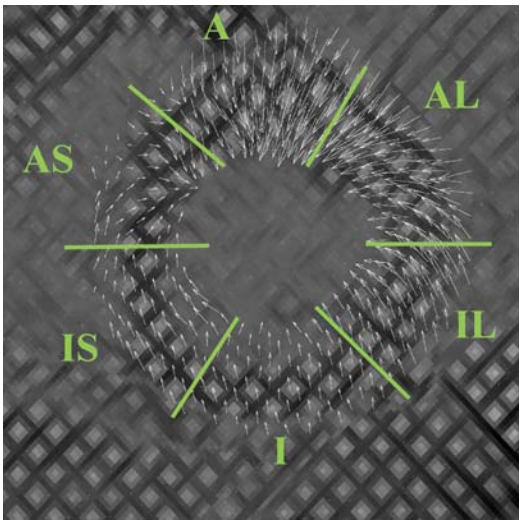

(a)

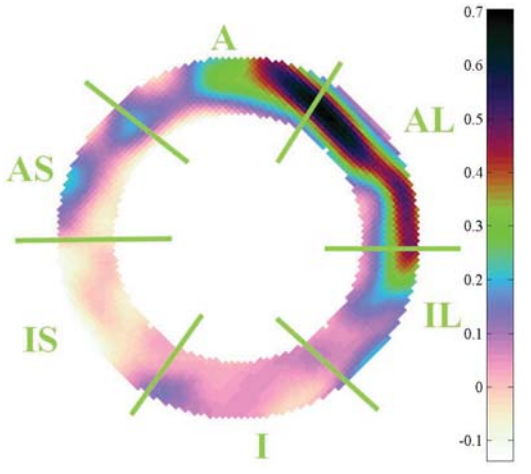

(b)

Figure 15: (a) Lagrangian motion field at end-systole frame. (b) Radial deformation E_{rr} of (a).

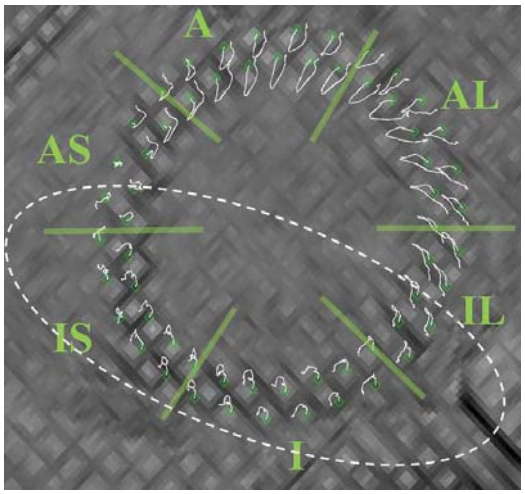

(a)

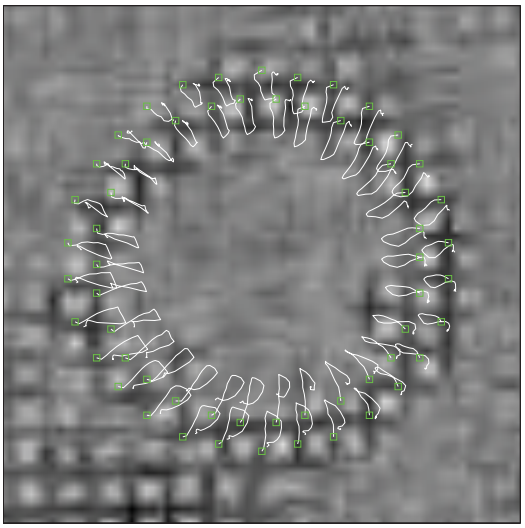

(b)

Figure 16: Trace of the myocardium local points on short-axis image sequence. (a) The region in the white dashed circle of the myocardium has shorter and non-smooth traces than the normal region at the myocardium segments A and AL, which indicates the possible myocardium pathologies. (b) A healthy case from a volunteer. All the tracing points represent the same tendency of contraction/dilation.

Furthermore, by applying the proposed method to two clinical cases with pathologies, we presented the radial deformation on end-systole frames as well as the local region tracking results of the myocardium. Our results discriminate between the different motion behaviors of the myocardium local regions. We also highlight that the local tracking results are potentially a useful indicator for the abnormalities of cardiac motion. In future work, an extension to 3D data application based on hypercomplex analytical signals and their phases will be studied.

Acknowledgments

This work was performed in the framework of the LABEX PRIMES (ANR-11-LABX-0063) and LABEX CELYA (ANR-

10-LABX-0060) of Université de Lyon, within the program "Investissements d'Avenir" (ANR-11-IDEX-0007) operated by the French National Research Agency (ANR). This work was partially supported by ANR-11-LABX-0040-CIMI in the program ANR-11-IDEX-0002-02 of the University of Toulouse and 3DSTRAIN ANR-11-TecSan-002 project.

References

Alessandrini, M., Basarab, A., Liebgott, H., Bernard, O., 2013. Myocardial motion estimation from medical images using the monogenic signal. IEEE Trans. Image Process. 22, 1084–1095.

Arif, O., Sundaramoorthi, G., Hong, B.W., Yezzi, A., 2014. Tracking via motion estimation with physically motivated inter-region constraints. IEEE Trans. Med. Imag. .

Arts, T., Prinzen, F., Delhaas, T., Milles, J., Rossi, A., Clarysse, P., 2010. Mapping displacement and deformation of the heart with local sine-wave modeling. IEEE Trans. Med. Imag. 29, 1114–1123.

Axel, L., Dougherty, L., 1989. MR imaging of motion with spatial modulation of magnetization. Radiology 171, 841–845.

Baker, S., Roth, S., Scharstein, D., Black, M., Lewis, J.P., Szeliski, R., 2007. A database and evaluation methodology for optical flow, in: IEEE Int. Conf. Computer Vision, pp. 1–8.

Baker, S., Scharstein, D., Lewis, J.P., Roth, S., Black, M.J., Szeliski, R., 2011. A database and evaluation methodology for optical flow. Int. J. Comput. Vis. 92, 1–31.

Basarab, A., Liebgott, H., Delachartre, P., 2009. Analytic estimation of subsample spatial shift using the phases of multidimensional analytic signals. IEEE Trans. Image Process. 18, 440–447.

Basarab, A., Liebgott, H., Morestin, F., Lyshchik, A., Higashi, T., Asato, R., Delachartre, P., 2008. A method for vector displacement estimation with ultrasound images and its application for thyroid nodular disease. Med. Image Anal. 12, 259–274.

Belytschko, T., Liu, W.K., Moran, B., Elkhodary, K., 2013. Nonlinear finite elements for continua and structures. John Wiley & Sons, New York.

Bülow, T., Sommer, G., 2001. Hypercomplex signals-a novel extension of the analytic signal to the multidimensional case. IEEE Trans. Signal Process. 49, 2844–2852.

Butler, D., Wulff, J., Stanley, G., Black, M., 2012. A naturalistic open source movie for optical flow evaluation, in: Proc. European Conference on Computer Vision, Springer. pp. 611–625.

Cerqueira, M.D., Weissman, N.J., Dilsizian, V., Jacobs, A.K., Kaul, S., Laskey, W.K., Pennell, D.J., Rumberger, J.A., Ryan, T., Verani, M.S., 2002. Standardized myocardial segmentation and nomenclature for tomographic imaging of the heart a statement for healthcare professionals from the cardiac imaging committee of the council on clinical cardiology of the american heart association. Circulation 105, 539–542.

Clarysse, P., Basset, C., Khouas, L., Croisille, P., Friboulet, D., Odet, C., Magnin, I.E., 2000. 2D spatial and temporal displacement field fitting from cardiac MR tagging. Med. Image Anal. , 253–268.

Clarysse, P., Tafazzoli, J., Delachartre, P., Croisille, P., 2011. Simulation based evaluation of cardiac motion estimation methods in tagged-MR image sequences. J. Cardiovasc. Magn. Reson. 13, P360.

Dallal, A., Khalifa, A., Fahmy, A., 2012. Accurate analysis of cardiac tagged MRI using combined HARP and optical flow tracking, in: Int. Conf. Biomedical Engineering, pp. 130–133.

Dietenbeck, T., Barbosa, D., Alessandrini, M., Jasaityte, R., Robesyn, V., D'ighthooge, J., Friboulet, D., Bernard, O., 2014. Whole myocardium tracking in 2D-echocardiography in multiple orientations using a motion constrained level-set. Med. Image Anal. 18, 500–514.

Felsberg, M., Sommer, G., 2001. The monogenic signal. IEEE Trans. Signal Process. 49, 3136–3144.

Fleet, D., Jepson, A., 1990. Computation of component image velocity from local phase information. Int. J. Comput. Vis. 5, 77–104.

Gabor, D., 1946. Theory of communication. J. Inst. Elect. Eng. 93, 429–457.

Geiger, A., Lenz, P., Urtasun, R., 2012. Are we ready for autonomous driving? the KITTI vision benchmark suite, in: IEEE Conf. Computer Vision and Pattern Recognition, pp. 3354–3361.

Guttman, M., Prince, J., McVeigh, E., 1994. Tag and contour detection in tagged mr images of the left ventricle. IEEE Trans. Med. Imag. 13, 74–88.

Hahn, S. L. asnd Snopek, K., 2011. The unified theory of n-dimensional complex and hypercomplex analytic signals. Bulletin of the Polish Academy of Sciences: Technical Sciences 59, 167–181.

Hahn, S.L., 1992. Multidimensional complex signals with single-orthant spectra. IEEE Proc. 80, 1287 –1300.

Hahn, S.L., Snopek, K.M., 2004. Comparison of properties of analytic, quaternionic and monogenic 2-D signals. WSEAS Trans. Comput. 3, 602–611.

Kar, J., Knutsen, A., Cupps, B., Pasque, M., 2014. A validation of two-dimensional in vivo regional strain computed from displacement encoding with stimulated echoes (DENSE), in reference to tagged magnetic resonance imaging and studies in repeatability. Ann. Biomed. Eng. 42, 541–554.

Luo, X.X., Fang, F., Lee, A.P.W., Sun, J.P., Li, S., Zhang, Z.H., Sanderson, J.E., Kwong, J.S., Zhang, Q., Wang, J., Yu, C.M., 2014. What can three-dimensional speckle-tracking echocardiography contribute to evaluate global left ventricular systolic performance in patients with heart failure? Int. J. Cardiol. 172, 132 – 137.

O'Dell, W.G., Moore, C.C., Hunter, W.C., Zerhouni, E.A., McVeigh, E.R., 1995. Three-dimensional myocardial deformations: calculation with displacement field fitting to tagged MR images. Radiology 195, 829–835.

Osman, N.F., Kerwin, W.S., Mcveigh, E.R., Prince, J.L., 1999. Cardiac motion tracking using CINE harmonic phase (HARP) magnetic resonance imaging. Magn. Reson. Med. 42, 1048–1060.

Oubel, E., De Craene, M., Hero, A.O., Pourmorteza, A., Huguet, M., Avegliano, G., Bijnens, B., Frangi, A.F., 2012. Cardiac motion estimation by joint alignment of tagged MRI sequences. Med. Image Anal. 16, 339–350.

Petitjean, C., Rougon, N., Cluzel, P., 2005. Assessment of myocardial function: a review of quantification methods and results using tagged MRI. J. Cardiovasc. Magn. Reson. 7, 501–516.

Prince, J., McVeigh, E., 1992. Motion estimation from tagged MR image sequences. IEEE Trans. Med. Imag. 11, 238–249.

Qian, Z., Liu, Q., Metaxas, D., Axel, L., 2011. Identifying regional cardiac abnormalities from myocardial strains using nontracking-based strain estimation and spatio-temporal tensor analysis. IEEE Trans. Med. Imag. 30, 2017–2029.

Ricco, S., Tomasi, C., 2012. Dense lagrangian motion estimation with occlusions, in: IEEE Conf. Computer Vision and Pattern Recognition, pp. 1800–1807.

Sun, D., Roth, S., Black, M., 2010. Secrets of optical flow estimation and their principles, in: IEEE Conf. Computer Vision and Pattern Recognition, pp. 2432–2439.

Sun, D., Roth, S., Black, M., 2014. A quantitative analysis of current practices in optical flow estimation and the principles behind them. Int. J. Comput. Vis. 106, 115–137.

Sun, F.r., Zhang, M.q., Jia, X.b., Wang, X.j., Yao, G.h., Zhang, Y., 2011. Region of interest tracking in real-time myocardial contrast echocardiography. J. Med. Syst. 35, 163–167.

Zang, D., Wietzke, L., Schmaltz, C., Sommer, G., 2007. Dense optical flow estimation from the monogenic curvature tensor, in: Scale Space and Variational Methods in Computer Vision. Springer Berlin Heidelberg. volume 4485 of *Lecture Notes in Comput. Sci.*, pp. 239–250.